Supporting Information

Morphology and doping engineering of sulfur-doped g-C_3N_4 hollow nanovesicles for boosting photocatalytic hydrogen production

Zifan Zhang [a, ‡], Changhui Song [a, ‡], Jipeng Fan [a], Zhijie Fang [c], Haitao Wang [a, b,*], Jing Zou [a,*]

[a] *School of Chemistry and Environmental Engineering, Novel Catalytic Materials of Hubei Engineering Research Center, Wuhan Institute of Technology, Wuhan 430205, China.*

[b] *Hubei Three Gorges Laboratory, Mazongling Road, Xiaoting District, Yichang 443000, Hubei, China.*

[c] *School of Electronics Engineering, Guangxi University of Science and Technology, Liuzhou 545006, China.*

‡ *These authors contributed equally to this work.*

*** Corresponding Author**

* E-mail: wanghaitao@wit.edu.cn (H. Wang); jingzou@wit.edu.cn (J. Zou)

Characterizations

A field emission scanning electron microscopy (FESEM, Gemini SEM 300, Germany Zeiss) with an energy-dispersive X-ray spectroscope (EDX) was employed to examine the surface morphology and element composition of as-obtained catalysts. The microstructure of all samples were examined by transmission electron microscopy (TEM) using a Tecnai G220 microscope operating at an acceleration voltage of 200 kV. A powder X-ray diffractometer (XRD, Bruker D8 ADVANCE diffractometer) was used to record the crystallographic structures of all samples. A X-ray photoelectron spectroscopy (XPS, ESCALAB XI^+ -600W, Thermo Fisher Scientific) was adopted to analyze the electronic structures and surface chemical components of as-obtained photocatalysts. The Brunner−Emmet−Teller (BET) measurements were recorded by N_2 adsorption-desorption isotherm on a surface analyzer (ASAP 2020 HD88, Micromeritics USA). The pore size distributions (PSD) were calculated according to the Barrett–Joyner–Halenda (BJH) method from the branch of adsorption isotherm.

Photoelectrochemical measurements

UV-Vis DRS were performed at a Carry5000 UV-Vis spectrophotometer (Agilent, USA). PL spectra were measured at an Edinburgh FLS980 (England) spectrophotometer. Transient photocurrent (TPC) responses and electrochemical impedance spectroscopy (EIS) measurements were evaluated on an electrochemical workstation (CHI660e Instruments) with a standard three-electrode photoelectrochemical cell, where an Ag/AgCl electrode, a platinum-wire electrode and a photocatalyst-coated glassy carbon electrode (GCE, 3 mm in diameter) were employed as the reference, counter, and working electrodes, respectively. Moreover, the potentials in this work were all converted to reversible hydrogen electrode (RHE, $E_{RHE} = E_{Ag/AgCl} + 0.1987 + 0.05916pH$). The electrolytes required for PC responses and EIS measurements were 0.5 $mol \cdot L^{-1}$ Na_2SO_4 and 5 $mmol \cdot L^{-1}$ potassium ferricyanide solution, respectively. In addition, a 10 W xenon lamp was employed as the light source for PC responses test.

Photocatalytic hydrogen evolution tests

Photocatalytic HER activity was obtained in an automatic on-line four trace gas analysis system (Labsolar-6A, Beijing PerfectLight) with a 300 W Xe lampas light source (cutoff filter $\lambda \geq 420$ nm). Before light exposure, 20 mg of catalysts, 3 wt% of platinum (provided by $H_2PtCl_6 \cdot 6H_2O$), and 10 mL of triethanolamine were ultrasonic mixed with 90 mL of deionized water at least 30 min. Especially, air must be removed from the photoreactor before testing. In addition, a circulating cooling water (below 10 °C) system was employed to eliminate thermal effect. H_2 was determined by an online gas chromatograph (GC9790II, China) accompanied with a thermal conductivity detector.

The corresponding AQE values were obtained according to the followed equations.

$$AQE(\%) = \frac{number\ of\ reacted\ electrons}{number\ of\ incident\ photons} \times 100\%$$

$$= \frac{2 \times number\ of\ evolved\ H_2\ molecules}{number\ of\ incident\ photons} \times 100\%$$

Details of theoretical calculations

DFT calculations were realized by using the CASTEP module of VASP. The exchange-correlation function in the form of Perdew-Burke-Ernzerhof was employed to study the surfaces of CN and HV-SCN. The Brillouin zone was sampled by Monkhorst Pack method (3 × 3 × 1 *k*-point grid). Moreover, the semiempirical dispersion correction of the Grimme scheme was considered for geometric optimization of CN and HV-SCN. Therein, the total energy of convergence criterion and the maximum force are 1.0×10^{-5} eV·atom^{-1} and 0.03 eV·Å^{-1}, respectively. The maximum displacement and stress and are 1.0×10^{-3} Å and 0.05 GPa, respectively.

The free energy calculation of hydrogen adsorption (ΔG_{H*}) was defined by Nørskovetals' hydrogen electrode model as follows:

$$\Delta G_{H*} = \Delta E_{H*} + \Delta E_{ZPE} - T\Delta S$$

Where ΔE, ΔE_{ZPE}, and ΔS respectively represent the changes of electronic energy, zero-point energy, and entropy that caused by adsorption of hydrogen. The ideal ΔG_{H*} is near zero, which could balance the adsorption and desorption of hydrogen reaction.

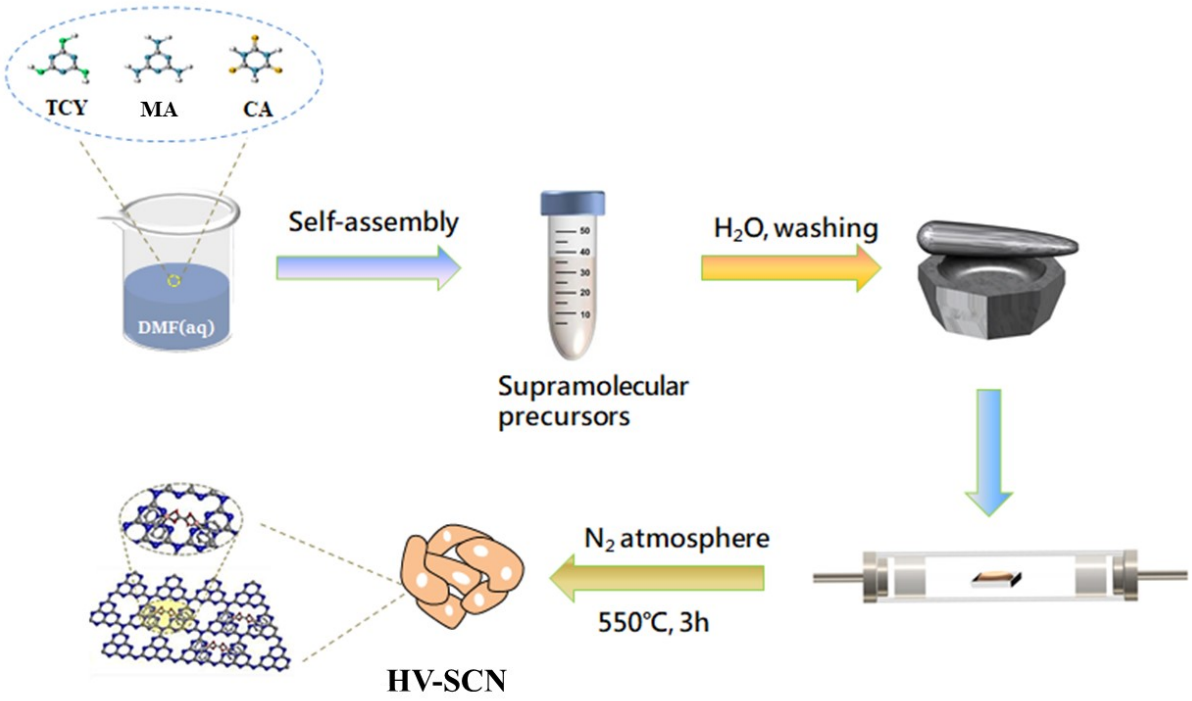

Figure S1. Schematic illustration of the preparation process of HV-SCN.

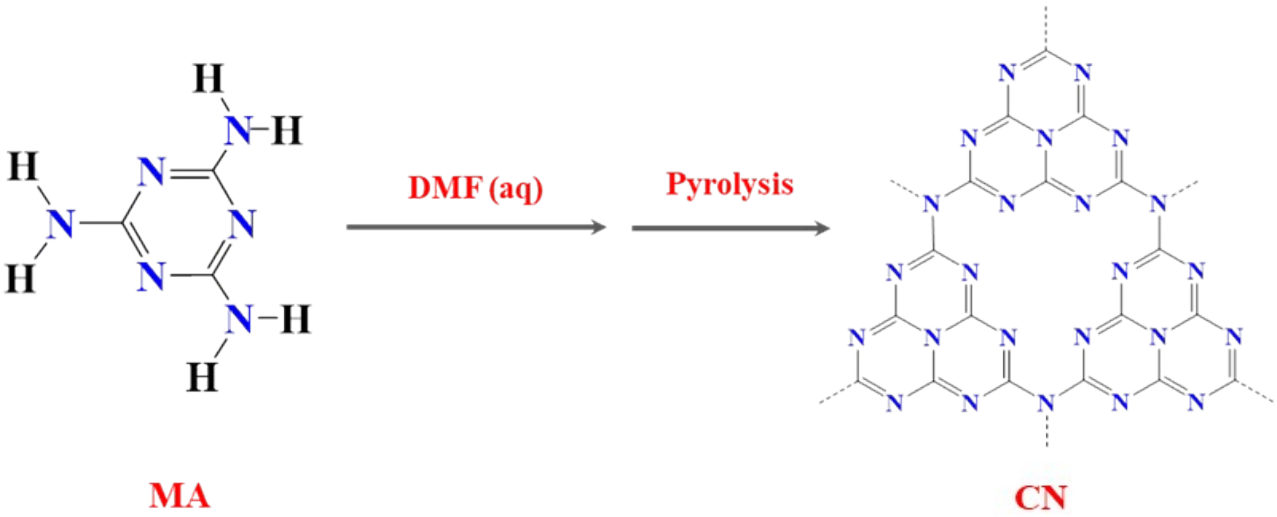

Figure S2. Schematic illustration of CN sample.

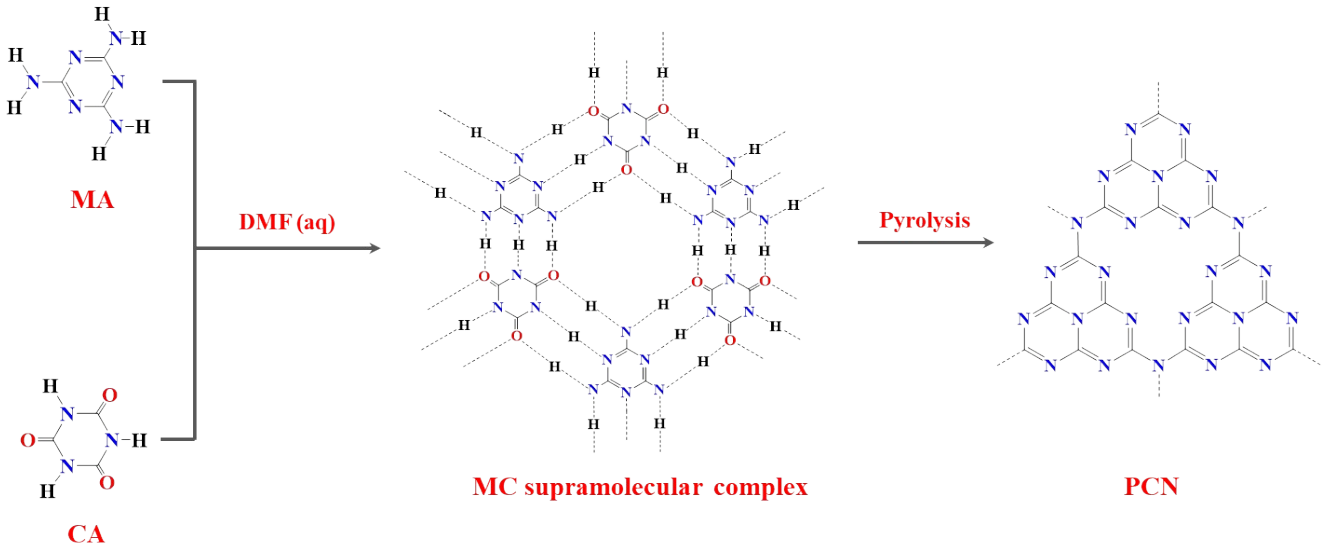

Figure S3. The pre-assembly formation of PCN sample.

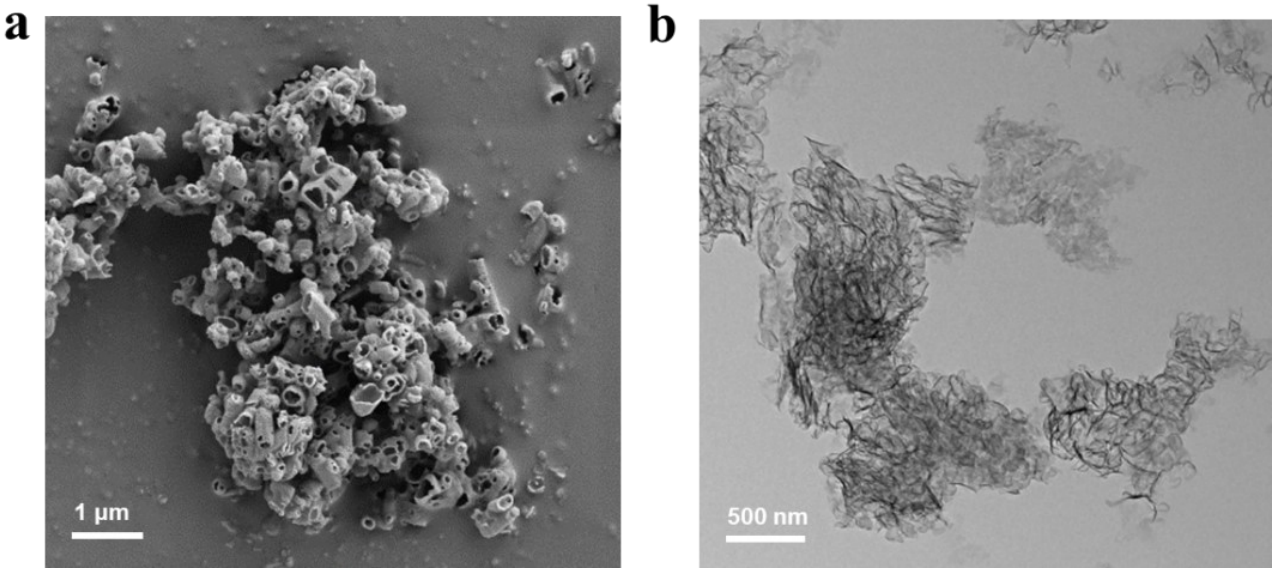

Figure S4. (a) SEM and (b) TEM images of HV-SCN.

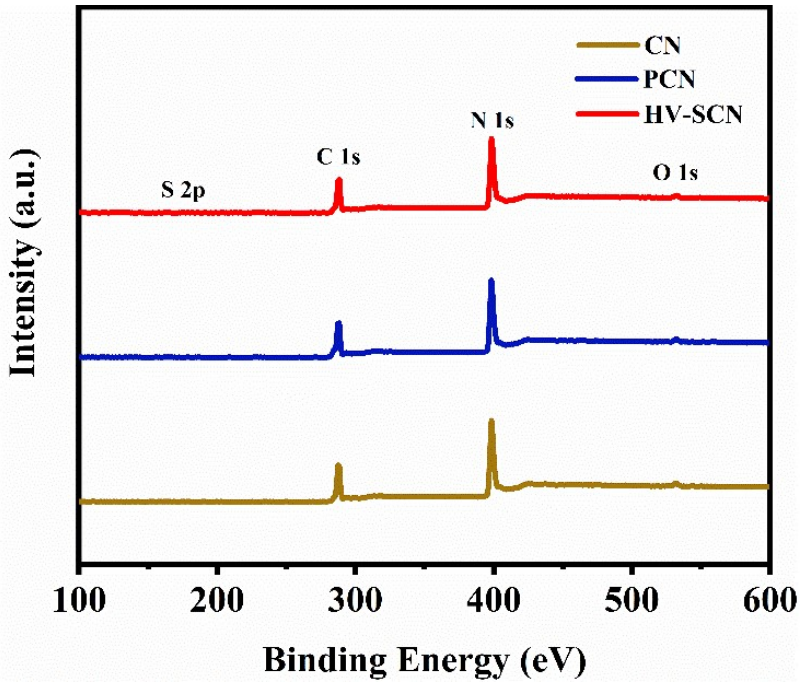

Figure S5. XPS survey spectra of CN, PCN and HV-SCN.

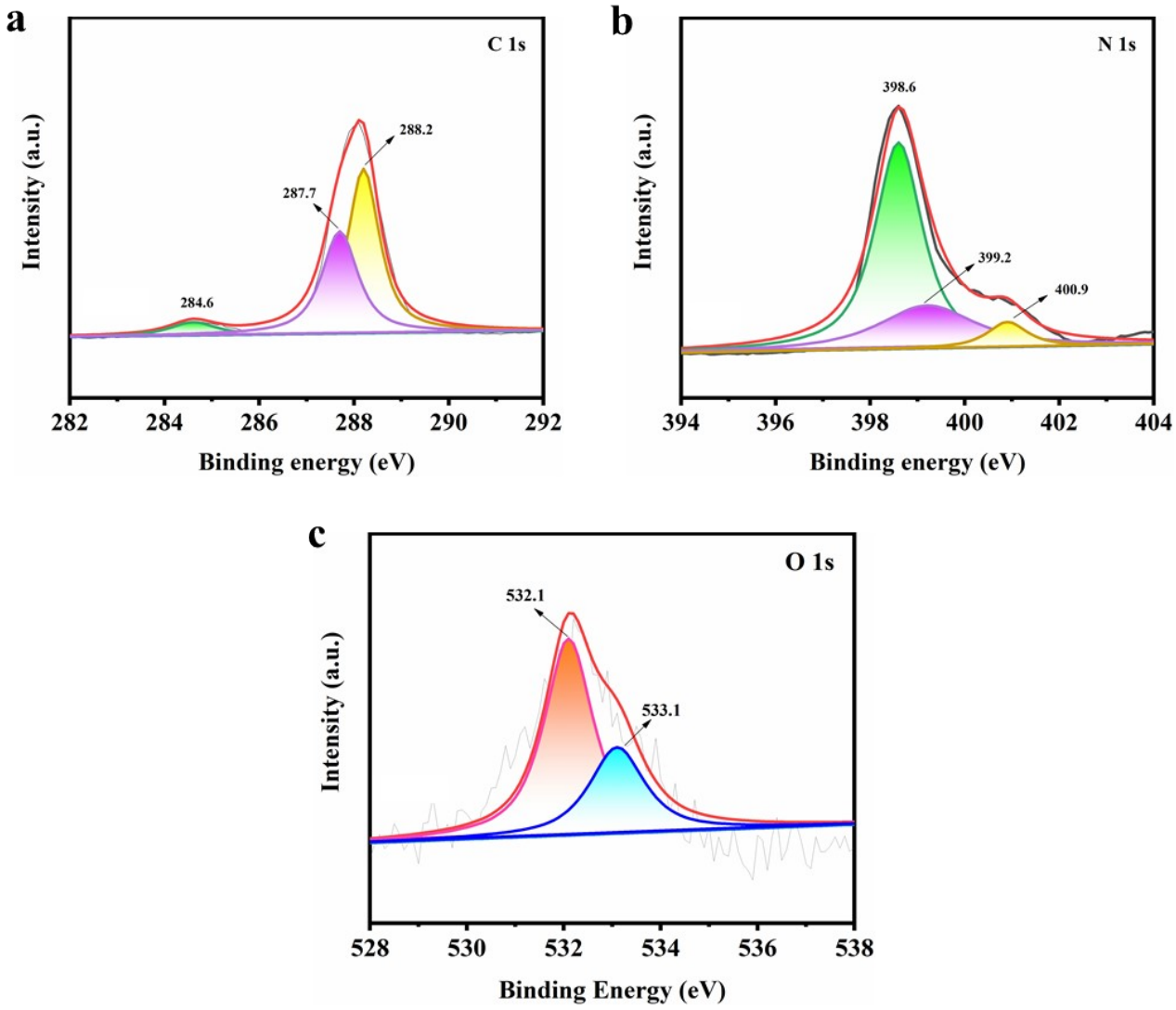

Figure S6. (a) High-resolution XPS spectra of C 1s, (b) N 1s and (c) O 1s for CN.

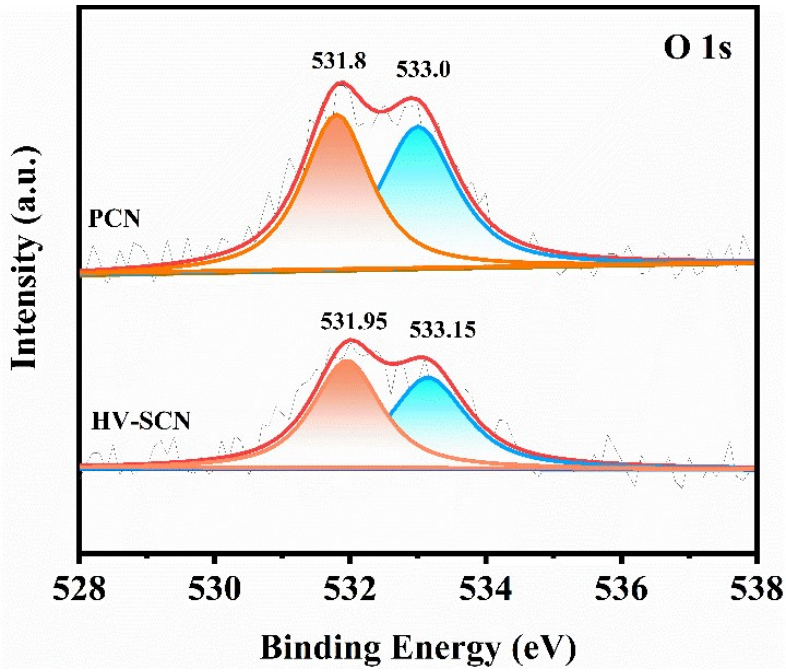

Figure S7. High-resolution XPS spectra of O 1s for PCN and HV-SCN.

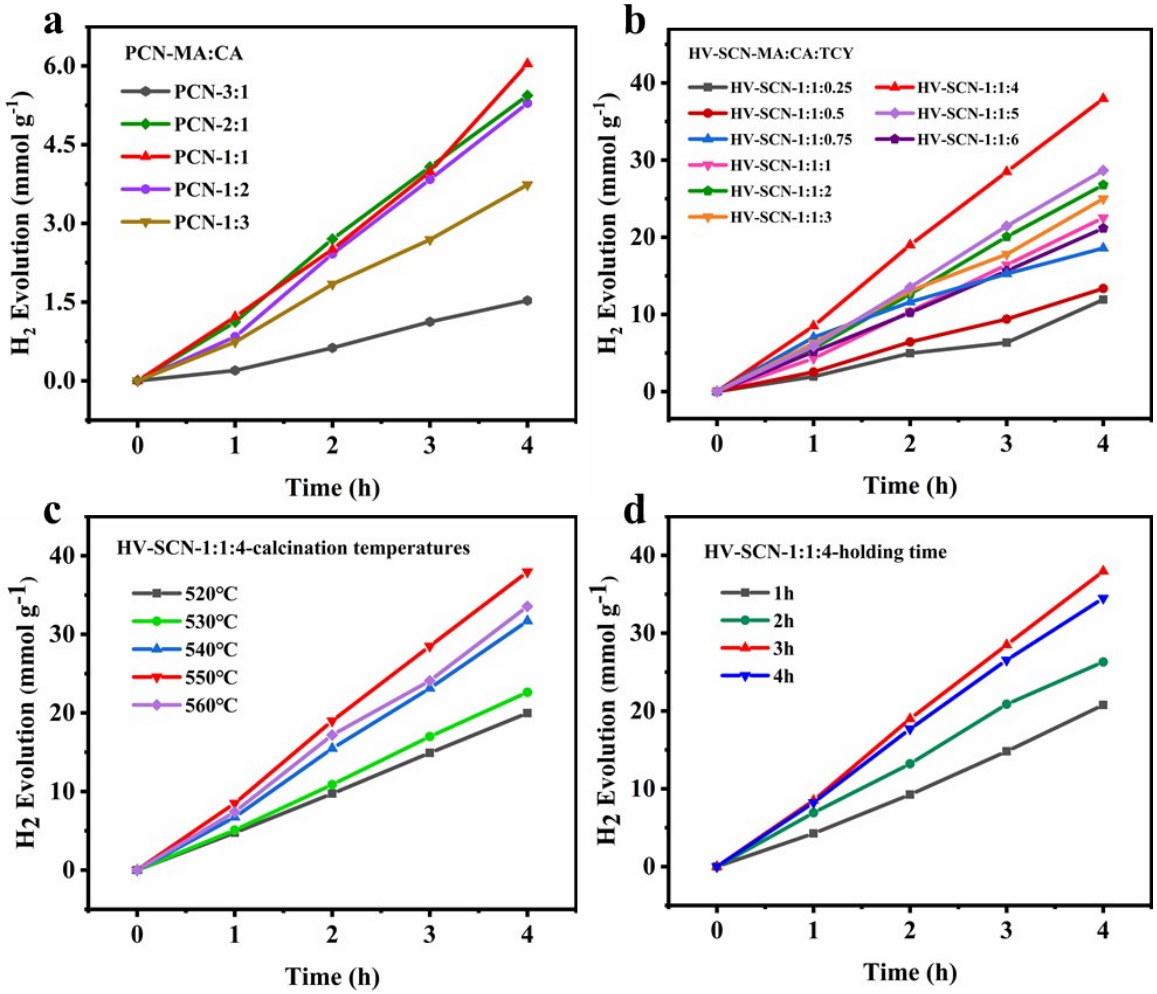

Figure S8. (a) Photocatalytic HER performance of PCN and (b) HV-SCN obtained at different precursor ratios. (c) Photocatalytic HER performance of HV-SCN obtained at different calcination temperatures. (d) Photocatalytic HER performance of HV-SCN obtained at different holding times.

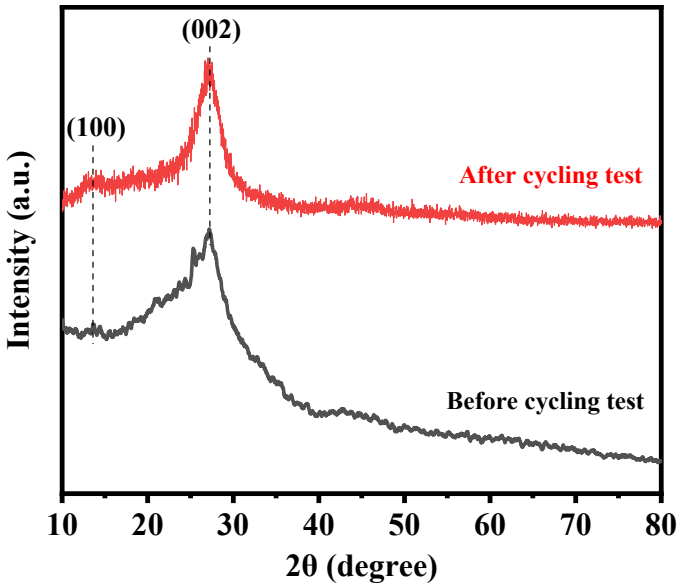

Figure S9. XRD patterns of HV-SCN before and after 24h continuous photocatalytic HER testing.

The (100) and (002) peaks of HV-SCN do not shift after stability testing. Moreover, the peak shape does not change significantly. The result proves the good structural integrity of developed HV-SCN catalyst.

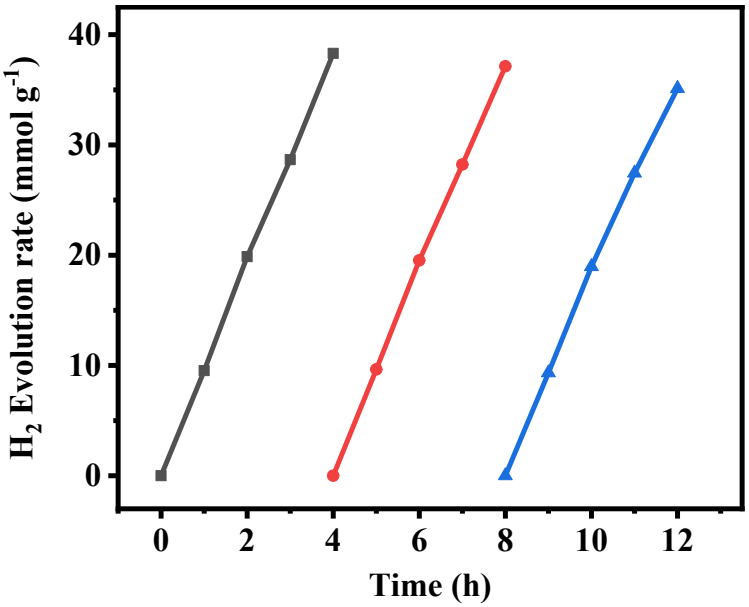

Figure S10. The photocatalytic stability of the HV-SCN after resting in a dry environment for 40 days.

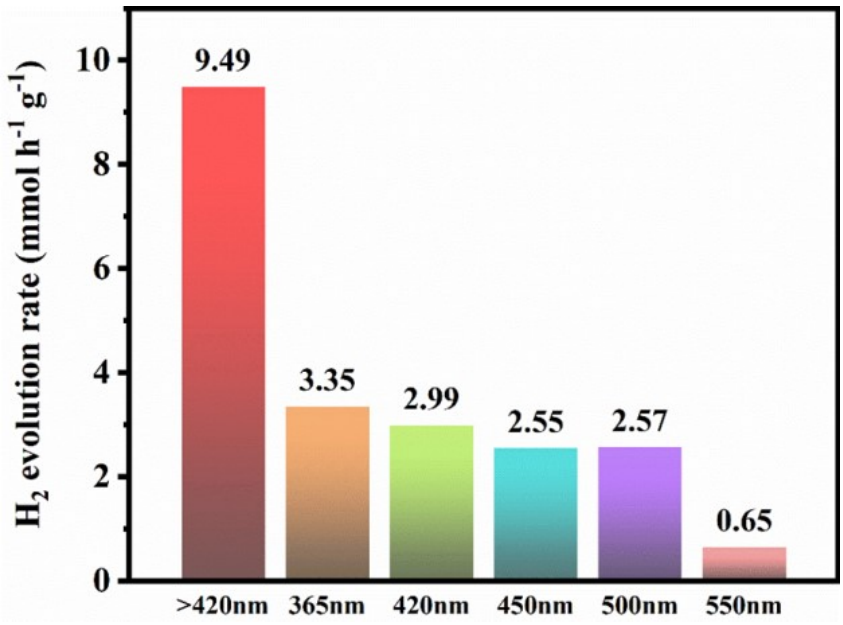

Figure S11. Photocatalytic H_2 evolution rate of HV-SCN at different wavelengths.

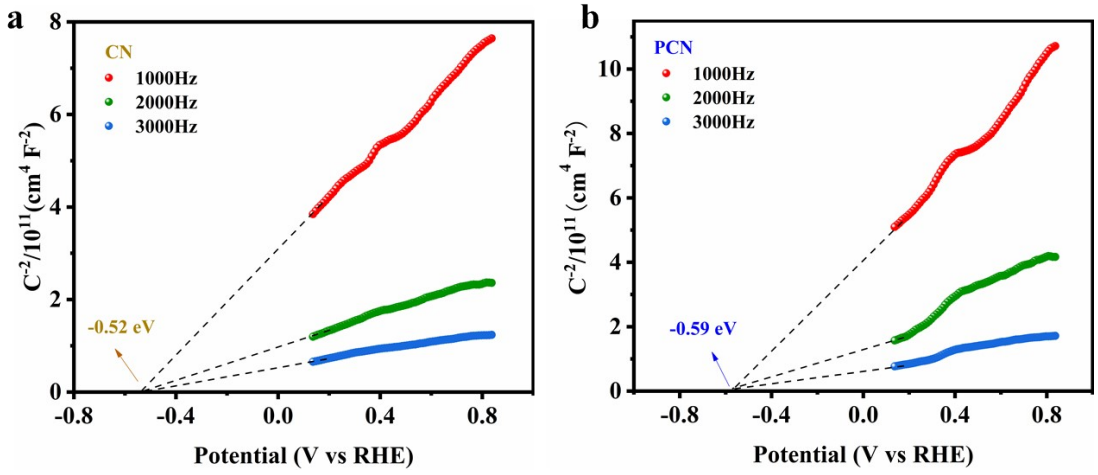

Figure S12. M-S plots of CN and PCN obtained at different frequencies.

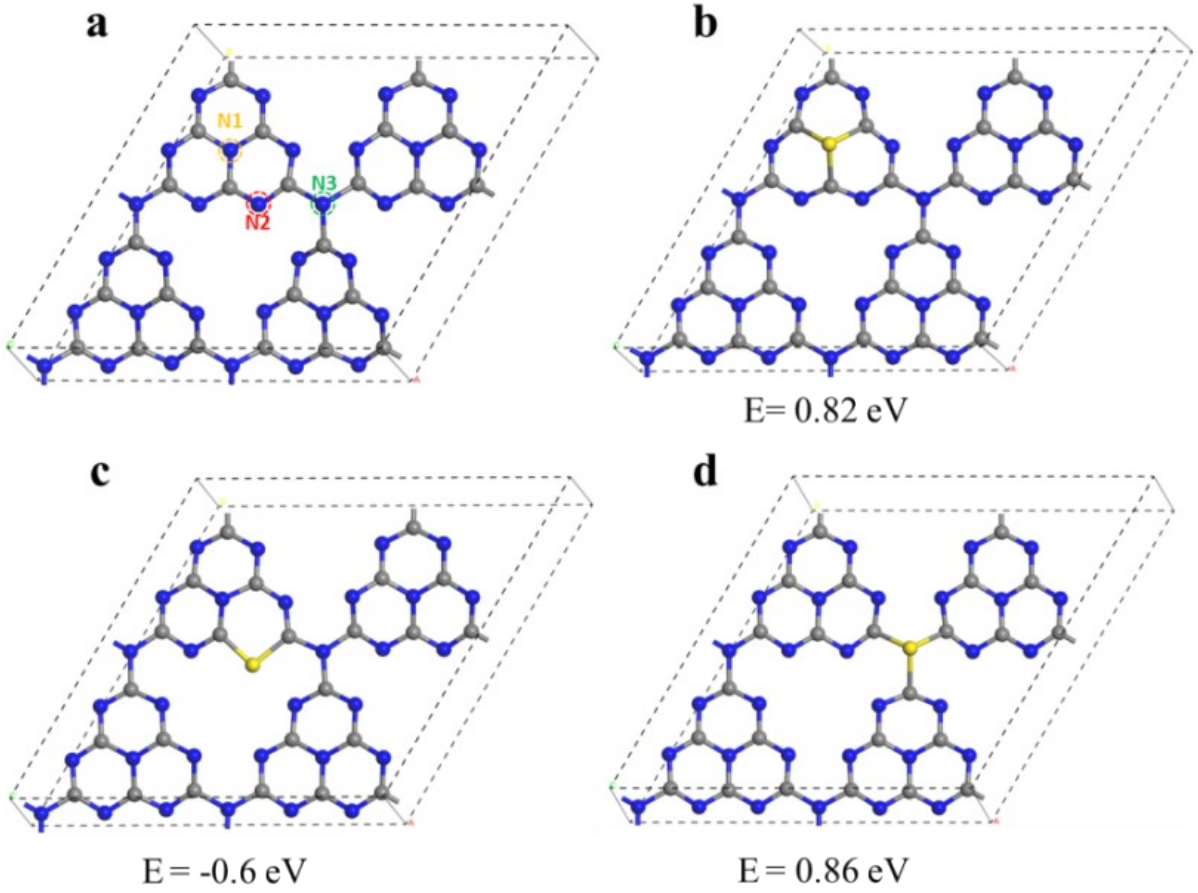

Figure S13. (a) Structure diagram of S-doping of different N-Sites for CN, and (b-d) the corresponding formation energy of different S-doping for CN.

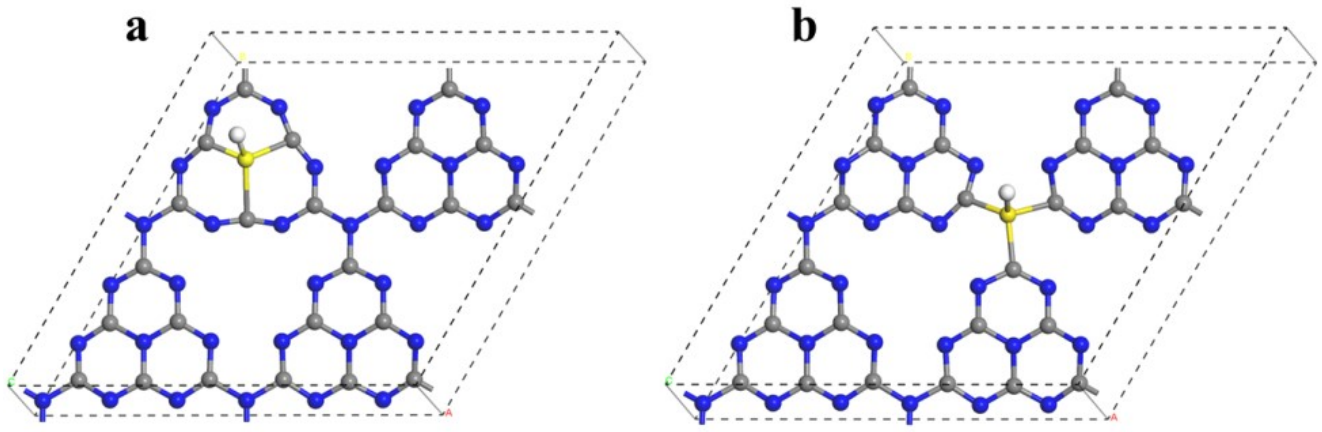

Figure S14. Optimized adsorption structures of H* intermediate at different S active sites of HV-SCN.

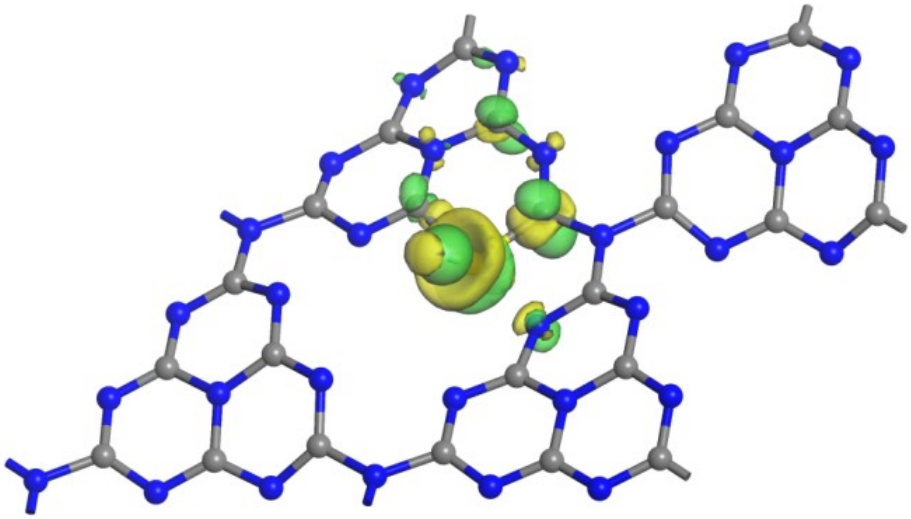

Figure S15. Top view of charge density difference for HV-SCN.

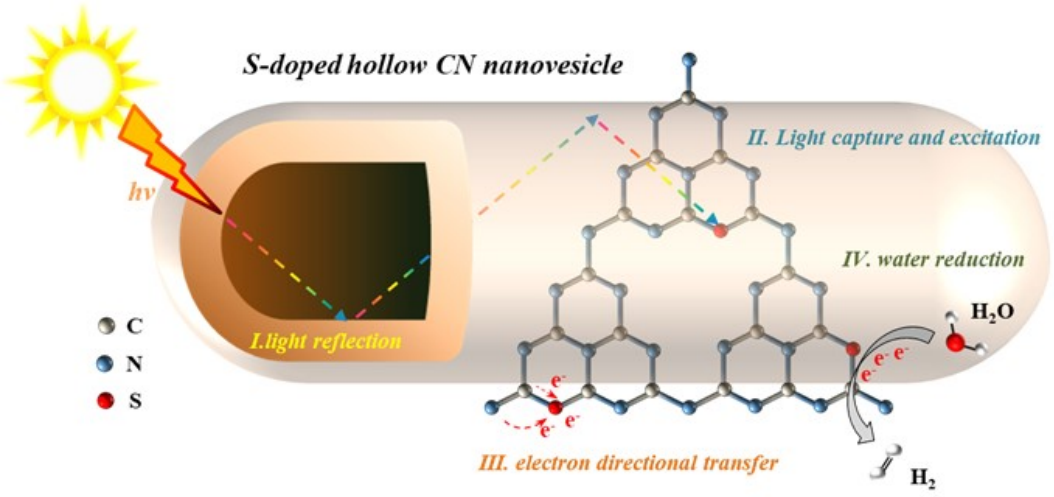

Figure S16. Schematic of the photocatalytic H_2 evolution mechanism of HV-SCN.

Table S1. Specific surface area and total pore volume of CN, PCN and HV-SCN.

Samples	S_{BET} ($m^2 g^{-1}$)	V_{Pore} ($cm^3 g^{-1}$)
CN	5.08	0.029
PCN	49.94	0.334
HV-SCN	70.93	0.405

Table S2. The EA results of CN, PCN and HV-SCN.

Samples	C (at.%)	N (at.%)	S (at.%)	C/N
CN	33.99	59.72	\	0.569
PCN	33.62	58.62	\	0.574
HV-SCN	32.81	56.49	0.15	0.581

Table S3. The XPS results of CN, PCN and HV-SCN.

Samples	C (at.%)	N (at.%)	O (at.%)	S (at.%)
CN	40.94	56.59	2.47	\
PCN	41.91	54.83	3.26	\
HV-SCN	42.47	54.52	2.78	0.23

Table S4. The S 2p XPS results of HV-SCN.

Samples	Peak	Binding energy (eV)	Assignment	FWHM (eV)	Area (Arb. unit)	ratio
HV-SCN	S 2p	164.3	S-C	2	446.97	0.809
		168.3	S-O	2.1	105.705	0.191

Table S5. The C 1s XPS results of CN, PCN and HV-SCN.

Samples	Peak	Binding energy (eV)	Assignment	FWHM (eV)	Area (Arb. unit)	ratio
CN	C 1s	284.6	C-C	1.15	6561	0.063
		287.7	$C\text{-}NH_2$	0.9	39744.98	0.385
		288.2	N-C=N	0.8	56967.81	0.552
PCN		284.6	C-C	1.15	10000	0.101
		287.8	$C\text{-}NH_2$	0.9	40582.35	0.407
		288.3	N-C=N	0.8	49057.91	0.492
HV-SCN		284.6	C-C	1.15	10000	0.099
		287.8	$C\text{-}NH_2$	0.9	44886.95	0.446
		288.3	N-C=N	0.8	45882.82	0.455

Table S6. The N 1s XPS results of CN, PCN and HV-SCN.

Samples	Peak	Binding energy (eV)	Assignment	FWHM (eV)	Area (Arb. unit)	ratio
CN	N 1s	398.6	C-N=C	1.2	162740.6	0.659
		399.2	$N-(C)_3$	2.9	67716	0.274
		400.9	$C-NH_2$	1	16430.29	0.067
PCN		398.6	C-N=C	1.2	86214.89	0.604
		399.2	$N-(C)_3$	2.9	49097.09	0.344
		400.9	$C-NH_2$	1	7511.512	0.052
HV-SCN		398.6	C-N=C	1.2	79994.01	0.536
		399.2	$N-(C)_3$	2.9	62189.59	0.417
		400.9	$C-NH_2$	1	7087.209	0.047

Table S7. The O 1s XPS results of CN, PCN and HV-SCN.

Samples	Peak	Binding energy (eV)	Assignment	FWHM (eV)	Area (Arb. unit)	ratio
CN	O 1s	532.1	adsorb oxygen	1.2	5347.007	0.670
		533.1	adsorbed water	1.35	2638.99	0.330
PCN		531.8	adsorb oxygen	1.2	5566.888	0.493
		533	adsorbed water	1.35	5722.988	0.507
HV-SCN		531.95	adsorb oxygen	1.2	3864.309	0.512
		533.15	adsorbed water	1.35	3669.809	0.478

Table S8. Comparison of photocatalytic HER activities of other S-doped CN catalysts reported recently.

Catalysts	Loading (mg)	Sacrificial agents	Light Source	Co-catalysts	H_2 evolution rate (mmol g^{-1} h^{-1})	Ref.
SPCN0.1	50	10 vol% TEOA	300 W Xe lamp (420 nm cut)	3 wt% Pt	4.20	[1]
HS-SPHI-650	50	10 vol% TEOA	300 W Xe lamp (420 nm cut)	2 wt% Pt	3.58	[2]
SCN/NiS-1	20	10 vol% TEOA	300 W Xe lamp (400 nm cut)	\	0.70	[3]
0.36-SUCN	20	10 vol% TEOA	300 W Xe lamp	2 wt% Pt	8.07	[4]
S-g-C_3N_4-E	20	10 vol% TEOA	300 W Xe lamp (420 nm cut)	3 wt% Pt	5.55	[5]
S-g-C_3N_4-D-1	20	10 vol% TEOA	300 W Xe lamp (420 nm cut)	3 wt% Pt	5.65	[6]
6Sr-SCN	10	17 vol% TEOA	500 W Xe lamp (420 nm cut)	3 wt% Pt	1.39	[7]
SCN-tm/CN	50	10 vol% TEOA	300 W Xe lamp (420 nm cut)	3 wt% Pt	5.41	[8]
$SCN_{0.8}$	20	10 vol% lactic acid	300 W Xe lamp (AM1.5G)	2 wt% Pt	3.93	[9]
S-g-C_3N_4-D-2	20	10 vol% TEOA	300 W Xe lamp (420 nm cut)	3 wt% Pt	3.11	[10]
g-CN-TM1	10	10 vol% TEOA	300 W Xe lamp (420 nm cut)	0.5 wt% Pt	4.43	[11]
S-CN(0.1)	50	10 vol% TEOA	300 W Xe lamp (420 nm cut)	3 wt% Pt	6.23	[12]
S-CN/$Pt_{0.3}$	100	20 vol% methanol	300 W Xe lamp	\	0.74	[13]
SS-CN	50	20 vol% TEOA	300 W Xe lamp (420 nm cut)	1 wt% Pt	0.98	[14]
HV-SCN	**20**	**10 vol% TEOA**	**300 W Xe lamp (420 nm cut)**	**3 wt% Pt**	**9.49**	**This work**

Table S9. Dynamics analysis of emission decay for different photocatalysts.

Sample	τ_1 (ns)	A_1	τ_2 (ns)	A_2	τ_{ave} (ns)
CN	1.285	1947840.0	9.539	844.7	1.311
PCN	1.523	593575.4	9.604	1319.1	1.641
HV-SCN	1.843	230365.4	8.981	2003.5	2.175

Table S10. fs-TAS results of CN , PCN and HV-SCN.

Sample	τ_1 (ns)	A_1	τ_2 (ns)	A_2	R^2
CN	10.17	1.344	163.78	0.422	0.99051
PCN	4.24	0.285	118.88	4.202	0.99966
HV-SCN	3.42	0.397	120.58	4.151	0.9994

Supplementary Reference

[1] Y. Jiao, M. Liu, J. Qin, et al., Sulfur/phosphorus doping-mediated morphology transformation of carbon nitride from rods to porous microtubes with superior photocatalytic activity. J. Colloid Interface Sci. **2022**, 608, 1432-1440.

[2] Y. Gao, Y. Li, L. Shangguan, et al., Optimizing the band structure of sponge-like S-doped poly(heptazine imide) with quantum confinement effect towards boosting visible-light photocatalytic H_2 generation. J. Colloid Interface Sci. **2023**, 644, 116-123.

[3] G. Zhou, Z. Zhou, Y. Xia, et al., Synchronous synthesis of S-doped carbon nitride/nickel sulfide photocatalysts for efficient dye degradation and hydrogen evolution. Appl. Surf. Sci. **2023**, 608, 154974.

[4] X. Wu, D. Li, B. Luo, et al., Molecular-level insights on NIR-driven photocatalytic H_2 generation with ultrathin porous S-doped g-C_3N_4 nanosheets. Appl. Catal., B **2023**, 325, 122292.

[5] J. Jiang, Z. Xiong, H. Wang, et al., Sulfur-doped g-C_3N_4/g-C_3N_4 isotype step-scheme heterojunction for photocatalytic H_2 evolution. J. Mater. Sci. Technol **2022**, 118, 15-24.

[6] H. Wang, J. Jiang, L. Yu, et al., Tailoring advanced N-defective and S-doped g-C_3N_4 for photocatalytic H_2 evolution. Small **2023**, 19, e2301116.

[7] F. Liu, W. Li, L. Wang, et al., Sulfur- and strontium-doped graphitic carbon nitride for efficient photocatalytic hydrogen evolution. ACS Appl. Energy Mater **2022**, 5, 15834-15843.

[8] Y. Gu, Y. Li, H. Feng, Y. Han, Z. Li, Built-in electric field induced S-scheme g-C_3N_4 homojunction for efficient photocatalytic hydrogen evolution: Interfacial engineering and

morphology control. Nano Res **2024**, 17, 4961-4970.

[9] S. Lin, B. Wu, Q. Li, et al., Rod-shaped aggregates of sulfur-doped carbon nitride nanosheets for enhanced photocatalytic hydrogen evolution. Science China Materials **2023**, 66, 4669-4679.

[10] J. Zou, G. Liao, J. Jiang, et al., In-situ construction of sulfur-doped g-C_3N_4/defective g-C_3N_4 Iso-type step-scheme heterojunction for boosting photocatalytic H_2 evolution. Chin. J. Struct. Chem **2022**, 41, 2201025-2201033.

[11] L. Niu, J. Du, X. Tian, et al., Facile steam activation route to synthesize S-doped graphitic polymeric carbon nitride nanosheets for increased photocatalytic H_2 generation. Mater. Lett. **2021**, 300, 130120.

[12] L. Luo, J. Ma, K. Wang, et al., Ultrathin sulfur-doped holey carbon nitride nanosheets with superior photocatalytic hydrogen production from water. Appl. Catal., B **2021**, 284, 119742.

[13] Z. Li, Y. Yao, X. Gao, H. Bai, X. Meng, Interfacial charge transfer and enhanced photocatalytic mechanisms for Pt nanoparticles loaded onto sulfur-doped g-C_3N_4 in H_2 evolution. Mater. Today Energy **2021**, 22, 100881.

[14] C. Feng, L. Tang, Y. Deng, et al., A novel sulfur-assisted annealing method of g-C_3N_4 nanosheet compensates for the loss of light absorption with further promoted charge transfer for photocatalytic production of H_2 and H_2O_2. Appl. Catal., B **2021**, 281, 119539.